Journal of Modern Optics

Bispectral Imaging Through Unknown Deterministic Aberrations

Donald T. Miller [a]; Doo Jin Cho [ab]; G. Michael Morris [a]; David R. Williams [a]
[a] The Institute of Optics, University of Rochester, Rochester, New York, USA
[b] Department of Physics, Ajou University, Suwon, Korea

PLEASE SCROLL DOWN FOR ARTICLE

Bispectral imaging through unknown deterministic aberrations

DONALD T. MILLER, DOO JIN CHO†,
G. MICHAEL MORRIS and DAVID R. WILLIAMS

The Institute of Optics, University of Rochester, Rochester,
New York 14627, USA

Abstract. When the deterministic aberrations are known in an optical system, traditional de-blurring methods are effective. However, when the aberrations are difficult to quantify, such as telescope aberrations or the aberrations in the human eye, other methods are needed. One potential method for de-blurring an image that is formed from a system with unknown aberrations is the bispectral imaging method. It is a promising way to remove the effects of deterministic aberrations when random aberrations are present or artificially introduced into the system. Through computer simulations, we have found the optimal amount of random aberrations to have present in a system containing deterministic aberrations. This amount optimizes the image quality of the reconstruction at high light levels using 100 statistically independent aberrated images of the object. Defocus and several third-order aberrations were considered in the isoplanatic case. The performance of this method was characterized by reconstructing a point source and computing its Strehl ratio. These results are currently being used to incorporate the bispectral imaging method as part of a non-invasive technique to reconstruct high-resolution images of the back of the eye in human subjects.

1. Introduction

There is currently a wide variety of methods that remove the effect of deterministic aberrations in imaging systems [1–8]. Deterministic aberrations are aberrations that remain fixed in time; they characterize the performance of the optical system and, for example, include such third-order aberrations as coma, astigmatism, and spherical aberration. When the deterministic aberrations are known, traditional de-blurring methods, such as the Wiener filter [1], aberration compensating filters [2], and spatial filters [3] can be effective. However, when the aberrations are difficult to quantify, such as telescope aberrations or the aberrations in the human eye, other methods are needed.

One potential method for de-blurring an image that is formed from a system with unknown aberrations is the bispectral imaging method. This image recovery technique reconstructs the object's Fourier phase using a sequence of statistically independent aberrated images of the spatially incoherent object. For an optical system with only deterministic aberrations, a sequence of statistically independent images cannot be generated. To obtain such a sequence, a noise source, which induces time-varying fluctuations on the object's wavefront, must be present or

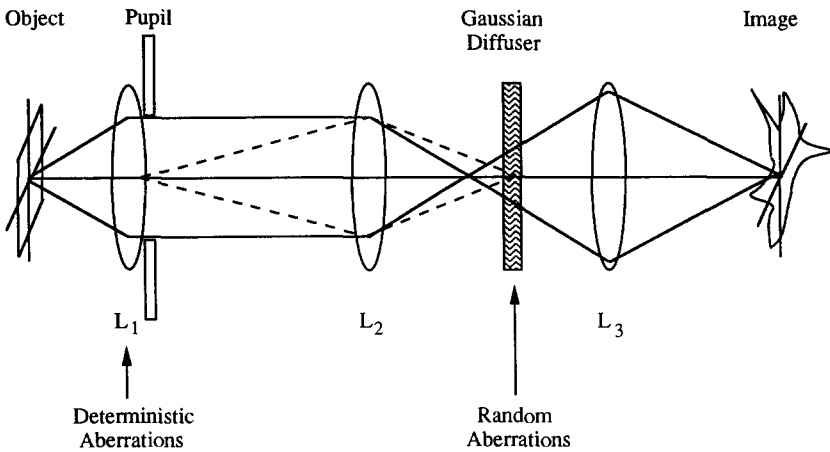† Present address: Department of Physics, Ajou University, Suwon, Korea.

Figure 1.   Illustration of how random aberrations are artificially introduced into the original system containing only deterministic aberrations. The system's pupil, which contains the deterministic aberrations, is imaged on to the Gaussian diffuser.

artificially introduced into the system's pupil. Such a noise source will be referred to in this paper as random aberrations. As will be shown, the random aberrations alter the effect the deterministic aberrations have on the bispectral transfer function of the system. For illustrative purposes, figure 1 depicts how random aberrations can be artifically introduced into the pupil of a system containing only deterministic aberrations.

The bispectral imaging technique has been found to be promising in removing the effects of deterministic aberrations when random aberrations are added to the system. This seemingly contradictory result (adding random aberrations to eliminate deterministic aberrations) can be understood as follows: the bispectral imaging method consists of computing a third-order moment of Fourier images containing three shifted versions of the same optical transfer function. The bispectral transfer function therefore contains the multiplication of six pupil functions (two pupil functions from each optical transfer function) whose relative shifts and orientations with respect to each other correspond to particular spatial frequencies in the bispectral transfer function. The six pupil functions are identical except that three are complex conjugates of the other three. When the shift between any two of the six pupil functions is zero, which corresponds to a complete overlap of the two pupils, and the two pupils are complex conjugates of each other, all points in the first pupil function are multiplied by their corresponding identical points in the second pupil function. Because the multiplied points are identical and complex conjugates, the deterministic aberrations in the two pupil functions completely cancel each other, and therefore the deterministic aberrations in these two pupil functions do not affect the bispectral transfer function. However, the deterministic aberrations in the remaining four pupil functions may still degrade the bispectral transfer function. Going further though, the six pupil functions can be shifted relative to each other to form three separate pairs, where each pair contains two pupil functions that completely overlap each other; this alignment of the six pupil functions is called phase closure [9]. When phase closure occurs, the deterministic aberrations in all six pupils completely cancel each other out and therefore cause no

degradation to the bispectral transfer function. Unfortunately these phase-closure terms contribute only a small fraction of the net contribution made to the bispectral transfer function at each spatial frequency; hence, in general, the bispectral transfer function is degraded by the presence of deterministic aberrations in the system. This is where the addition of random aberrations into the system is beneficial. The addition of random aberrations separates the complex wavefront at the pupil into many small statistically independent subsections. In effect, when these statistically independent subsections are sufficiently small, the non-phase-closure contributions to the bispectral transfer function are strongly suppressed; the phase-closure contributions, however, remain unaffected because the random aberrations, like the deterministic aberrations, cancel each other. Thus the random aberrations act as a 'filter' in the bispectral method that passes only the phase-closure contributions to the bispectral transfer function thereby removing the effects of the deterministic aberrations.

A detailed description of the phase-closure characteristic of the bispectral imaging technique in terms of the heuristic interferometric view was given by Roddier [9], who showed that the technique is insensitive to deterministic aberrations when random aberrations are present. Lohmann *et al.* [10] showed analytically that the bispectral transfer function remains real and positive out to the diffraction limit when deterministic aberrations and complex Gaussian-distributed, delta-correlated random aberrations are present. More realistic correlation lengths for the random aberrations were studied by Barakat and Ebstein [5] for the one-dimensional case. They modelled the random aberrations as a zero-mean, finite-variance Gaussian random process that modulated the phase of the wavefront. In the presence of even deterministic aberrations, such as defocus and spherical aberration, and Gaussian-distributed Gaussian-correlated random aberrations, Barakat and Ebstein found that the bispectral transfer function remains real and positive out to the diffraction limit as long as the variance of the Gaussian distribution for the random aberrations is not too small. In a more recent paper, Zhang and Dainty [11] computed the bispectral transfer function from a finite number of computer-generated, short-exposure, one-dimensional images in the presence of deterministic and random aberrations. A log-normal model was used to represent the complex amplitude of the random aberrations. They found that using a finite number of images produces an unwanted non-zero phase component in the bispectral transfer function; this non-zero phase component becomes more severe when deterministic aberrations are present. However, when a large number of short-exposure images are used, the non-zero phase component of the bispectral transfer function is effectively zero and their results then appear to agree with those of Barakat and Ebstein. Weigelt *et al.* [12] experimentally found high-resolution images could be obtained with the bispectral imaging method when atmosphere and telescope aberrations were simultaneously present. The work of these authors clearly demonstrates that the bispectral imaging technique is effective at removing the detrimental effects of deterministic aberrations when random aberrations are present. However, they do not address the problem of determining the optimal amount of random aberrations to artificially introduce into a system, containing only deterministic aberrations, to optimize the image quality of the reconstruction.

By performing a trial-and-error optimization method through computer simulations, we have found the amount of random aberrations that optimize image

quality in a system containing deterministic aberrations. The Strehl ratio is used in this paper to measure image quality. The optimal amount of random aberrations produces the maximum Strehl ratio of the reconstruction when imaging a point source through the system. The reconstructions were obtained at high light levels using 100 statistically independent images of the two-dimensional object. The point source was reconstructed using the bispectral imaging method in the presence of deterministic and Gaussian random aberrations. For a given type and amount of deterministic aberrations, the Strehl ratio of the reconstructed point spread function was compared for various standard deviations and correlation lengths of the Gaussian random aberrations.

The motivation to obtain these results has been a practical one. We are currently developing a non-invasive technique to reconstruct high-resolution images of the eye's fundus in human subjects. The fundus is the internal surface of the eye that is opposite the eye's pupil. The fundus includes such structures as the retina, optic disk, and pigment epithelium. This non-invasive technique incorporates the bispectral imaging method. The problem in imaging the eye's fundus through the optics of the eye is that the deterministic aberrations in the optics of the eye strongly blur many of the small-scale structures in the fundus. Such small-scale structures include individual cones and rods as well as blood vessels. Traditional de-blurring methods are not effective, since the aberrations in the optics of the eye are difficult to accurately quantify within a given individual and vary considerably between individuals [13, 14]. With the bispectral imaging method, only a rough estimate of the deterministic aberrations is required. Using the typical types and amounts of deterministic aberrations found in the average human eye, the results of this paper will help determine the values for the standard deviation and correlation length of the random aberrations that will be artificially introduced into the fundus imaging system to optimize the image quality of the reconstruction.

In section 2 the key quantities used in bispectral imaging are introduced. The characterization of the deterministic and random aberrations is given; this characterization is essentially that used by Barakat and Ebstein [5] and Goodman [15]. Next Barakat and Ebstein's integral representation of the bispectral transfer function is described. Their analytic expression of the bispectral transfer function illustrates the benefits that can be obtained by introducing random aberrations into a system containing deterministic aberrations. Results from the analytic expression of the bispectral transfer function are used in explaining the results obtained using the trial-and-error simulation. In section 3 the trial-and-error simulation is described. Finally, the results of the simulation are presented in section 4.

2. Theory of bispectral imaging

The theory of bispectral imaging has been well established [5, 9, 10]. Its key quantities are given in this section in order to introduce the notation as well as make later comparisons between the established theory and the results of the trial-and-error simulation. In addition, Barakat and Ebstein's integral representation of the bispectral transfer function is described. Their analytic expression is later used in explaining the results obtained using the trial-and-error simulation given in section 4. To simplify the notation, we will deal only with the one-dimensional case, although the analytic results can be readily extended to the two-dimensional case.

We start with a spatially incoherently illuminated, or self-luminous, quasi-monochromatic object. Assuming the system is linear and shift-invariant, the recorded image of the object can be expressed as

$$i(x) = \int h(x - x')o(x')\mathrm{d}x'. \tag{1}$$

The image $i(x)$ is the convolution between the object $o(x)$ and the point spread function $h(x)$. The Fourier transform of equation (1) is given by

$$I(u) = H(u)O(u), \tag{2}$$

where $I(u)$ is the Fourier transform of $i(x)$, $O(u)$ is the Fourier transform of $o(x)$, and $H(u)$ is the optical transfer function. The optical transfer function is defined as the autocorrelation of the pupil function $P(u)$:

$$H(u) = \int P\left(p + \frac{u}{2}\right) P^*\left(p - \frac{u}{2}\right) \mathrm{d}p. \tag{3}$$

The image bispectrum is defined as the multiplication of three Fourier image values at u, v, and $u + v$. It is expressed as

$$\langle I(u)I(v)I^*(u + v)\rangle = O(u)O(v)O^*(u + v)\langle H(u)H(v)H^*(u + v)\rangle, \tag{4}$$

where $\langle\,\rangle$ represents an ensemble over all possible realizations. To simplify the notation, equation (4) is written in the form

$$\langle I^{(3)}(u, v)\rangle = O^{(3)}(u, v)\langle T^{(3)}(u, v)\rangle, \tag{5}$$

where

$$\langle I^{(3)}(u, v)\rangle = \langle I(u)I(v)I^*(u + v)\rangle, \tag{6a}$$

$$O^{(3)}(u, v) = O(u)O(v)O^*(u + v), \tag{6b}$$

$$\langle T^{(3)}(u, v)\rangle = \langle H(u)H(v)H^*(u + v)\rangle, \tag{6c}$$

$\langle I^{(3)}(u, v)\rangle$ is the image bispectrum, $O^{(3)}(u, v)$ is the object bispectrum, and $\langle T^{(3)}(u, v)\rangle$ is the bispectral transfer function. The bispectral imaging method extracts diffraction-limited Fourier phase information of the object from the image bispectrum. When imaging through Gaussian random aberrations and recording a sufficient number of statistically independent images of the object, $\langle T^{(3)}(u, v)\rangle$ has zero phase and no zero points out to the diffraction limit [5]. As a result, the phase of the object bispectrum directly equals the phase of the image bispectrum in equation (5). This implies that the Fourier phase of the object can be recovered out to the diffraction limit without compensation for the system's transfer function. When the system contains deterministic aberrations, $\langle T^{(3)}(u, v)\rangle$ often contains non-zero phase as well as zero points; both non-zero phase and zero points are unwanted characteristics of $\langle T^{(3)}(u, v)\rangle$ because both cause blurring in the image. Non-zero phase is defined here as any phase value other than zero and π. Non-zero phase in $\langle T^{(3)}(u, v)\rangle$ blurs the image because it destroys the phase relationships between the spatial frequencies that form the object. Zero points in $\langle T^{(3)}(u, v)\rangle$ blur the image because they indicate a 180° phase reversal between spatial frequencies before and after the zero points. In addition, complete attenuation of the spatial frequencies at the zero points occurs in the image as well as high attenuation of the adjacent spatial frequencies, thus causing extremely small signal-to-noise ratios (SNRs) at these spatial frequencies.

Adding random aberrations into the system can remove some of these unwanted characteristics in the bispectral transfer function. The degree to which they are removed depends upon the standard deviation and correlation length of the random aberrations. However, this benefit of adding random aberrations into the system is not without a price. The drawback of adding random aberrations is that they reduce the overall magnitude of the bispectral transfer function. The stronger the random aberrations are, the smaller the magnitude of the bispectral transfer function becomes. Thus the SNR of the image bispectrum is reduced and can become the limiting factor in the quality of the reconstructed image. The problem then is to determine the standard deviation and correlation length of the random aberrations that will remove as much as possible these unwanted characteristics in $\langle T^{(3)}(u,v)\rangle$ caused by the deterministic aberrations, and at the same time maintain the SNR of the image bispectrum at acceptable levels.

For the trial-and-error simulation, the modelling of the aberrated media is essentially that used by Barakat and Ebstein [5] and by Goodman [15]. The deterministic wavefront aberrations $W(u)$ are located at the pupil of the system, but remain fixed in time. They characterize the performance of the optical system and multiply the wavefront by the phase factor $\exp(ikW(u))$, where $k = 2\pi/\lambda$ and λ is the wavelength of the incident light. In our study we consider defocus and third-order astigmatism, coma, and spherical aberration. In two dimensions these aberrations are defined as [16]

$$W(\mathbf{u}) = W_{020}u^2 + W_{022}u^2 \cos^2\theta + W_{031}u^3 \cos\theta + W_{040}u^4, \qquad (7)$$

where u and θ are polar coordinates in the pupil plane. Astigmatism and coma are both considered in the isoplanatic case, meaning the point spread function of the aberrated system is shift-invariant. Defocus, astigmatism, and spherical aberration are even aberrations because they contain an even power of u. All three induce zero phase in $H(u)$ and therefore $\langle T^{(3)}(u,v)\rangle$ likewise contains zero phase. On the other hand, coma is an odd aberration because it contains an odd power of u. Unlike the even aberrations, coma does induce non-zero phase in $H(u)$ and therefore induces non-zero phase in $\langle T^{(3)}(u,v)\rangle$.

The random aberrations are modelled as a random process of a thin random phase screen located at the pupil of the system that induces time-varying fluctuations on the object's wavefront. The random aberrations multiply the wavefront by the phase factor $\exp(ikZ(u))$, where $Z(u)$ represents a zero-mean, Gaussian random process:

$$\langle Z(u)\rangle = 0,$$

$$\langle Z(u_1)Z(u_2)\rangle = \sigma^2 r(u_1 - u_2). \qquad (8)$$

In equation (8) σ^2 is the variance of the Gaussian process $Z(u)$, and $r(u_1 - u_2)$ denotes the correlation coefficient of $Z(u)$. In our simulations, $r(u_1 - u_2)$ is taken to be of Gaussian form and is expressed as

$$r(u_1 - u_2) = \exp\left[-\frac{(u_1 - u_2)^2}{2\rho^2}\right], \qquad (9)$$

where $\sqrt{(2)}\rho$ is the correlation length of $Z(u)$. The parameters σ and ρ completely characterize the properties of the random aberrations.

Combining the effects of the random and deterministic aberrations, the pupil function $P(u)$ can be written as

$$P(u) = \exp\left[ik(Z(u) + W(u))\right]. \tag{10}$$

Substituting the pupil function, equation (10), into the optical transfer function, equation (3), yields the following expression for the optical transfer function of the system:

$$H(u) = \int \exp\left(ik\left[Z\left(p + \frac{u}{2}\right) - Z\left(p - \frac{u}{2}\right)\right]\right)\exp\left(ik\left[W\left(p + \frac{u}{2}\right) - W\left(p - \frac{u}{2}\right)\right]\right)dp. \tag{11}$$

Using equation (11) and equation (6 c), one finds that

$$\langle T^{(3)}(u,v)\rangle = \int\int\int\left\langle\exp\left(ik\sum_{m=1}^{6}Z_m\right)\right\rangle\exp\left(ik\sum_{m=1}^{6}W_m\right)dp_1dp_2dp_3. \tag{12}$$

In the first exponential term of the integrand, the Z_m terms are given by

$$Z_1 \equiv Z\left(p_1 + \frac{u}{2}\right) \qquad Z_2 \equiv -Z\left(p_1 - \frac{u}{2}\right),$$

$$Z_3 \equiv Z\left(p_2 + \frac{v}{2}\right) \qquad Z_4 \equiv -Z\left(p_2 - \frac{v}{2}\right), \tag{13}$$

$$Z_5 \equiv -Z\left(p_3 + \frac{u}{2} + \frac{v}{2}\right) \quad Z_6 \equiv Z\left(p_3 - \frac{u}{2} - \frac{v}{2}\right).$$

In the second exponential term, the W_m terms are given by

$$W_1 \equiv W\left(p_1 + \frac{u}{2}\right) \qquad W_2 \equiv -W\left(p_1 - \frac{u}{2}\right),$$

$$W_3 \equiv W\left(p_2 + \frac{v}{2}\right) \qquad W_4 \equiv -W\left(p_2 - \frac{v}{2}\right), \tag{14}$$

$$W_5 \equiv -W\left(p_3 + \frac{u}{2} + \frac{v}{2}\right) \quad W_6 \equiv W\left(p_3 - \frac{u}{2} - \frac{v}{2}\right).$$

Since $Z(u)$ is a zero-mean, Gaussian random process, equation (12) can be expressed as

$$\langle T^{(3)}(u,v)\rangle = \int\int\int \exp\left(-k^2\sigma^2 Q(p_1,p_2,p_3|u,v)\right)\exp\left(ik\sum_{m=1}^{6}W_m\right)dp_1dp_2dp_3, \tag{15}$$

where

$$Q(p_1,p_2,p_3|u,v) = 3 - r(u) - r(v) - r(u+v)$$

$$+ r\left(p_1 - p_2 + \frac{u}{2} - \frac{v}{2}\right) + r\left(p_1 - p_2 - \frac{u}{2} + \frac{v}{2}\right)$$

$$- r\left(p_1 - p_2 + \frac{u}{2} + \frac{v}{2}\right) - r\left(p_1 - p_2 - \frac{u}{2} - \frac{v}{2}\right)$$

$$+ r\left(p_1 - p_3 + u + \frac{v}{2}\right) + r\left(p_1 - p_3 - u - \frac{v}{2}\right)$$

$$+ r\left(p_2 - p_3 + \frac{u}{2} + v\right) + r\left(p_2 - p_3 - \frac{u}{2} - v\right)$$

$$-r\left(p_1-p_3+\frac{v}{2}\right)-r\left(p_1-p_3-\frac{v}{2}\right)$$

$$-r\left(p_2-p_3+\frac{u}{2}\right)-r\left(p_2-p_3-\frac{u}{2}\right).\tag{16}$$

The first exponential term in the integrand of equation (15) represents the contribution from the random aberrations. It is an exponentially decaying function that is real and positive; therefore, in the absence of deterministic aberrations, the bispectral transfer function will also be real and positive. The deterministic aberrations are represented by the second exponential term in the integrand. This term behaves in an oscillating manner. In the absence of random aberrations, this term induces a non-zero phase in $\langle T^{(3)}(u,v)\rangle$ for odd aberrations such as coma. For even aberrations, such as defocus, astigmatism, and spherical aberration, only zero phase is induced. In general, the deterministic aberrations will cause $\langle T^{(3)}(u,v)\rangle$ to have zero points and non-zero phase. Both are unwanted characteristics because they cause blurring in the image. For systems containing only deterministic aberrations, it is then apparent that the bispectral imaging method will be ineffective, since the method does not compensate for non-zero phase and zero points in the bispectral transfer function. Fortunately, if random aberrations are introduced into the system, the deterministic term in equation (15) is damped by an exponentially decaying function given by the first term in the integrand. Barakat and Ebstein found that if the variance of the random aberrations σ^2 is not too small and the correlation length $\sqrt{(2)}\rho$ is taken to be a typical atmospheric value, the deterministic term is damped sufficiently to cause the bispectral transfer function to be real and greater than zero up to the diffraction-limit cutoff frequency when even deterministic aberrations are present in the system. With the odd aberration coma and the same random aberrations present, they also found the bispectral transfer function to have non-zero phase and a magnitude greater than zero up to the diffraction-limit cutoff frequency.

The problem then becomes one of determining the values of σ and ρ that produce a bispectral transfer function that optimizes the object reconstruction for a system containing a given type and amount of deterministic aberrations. Assuming that optimizing the object reconstruction is strongly correlated with maximizing the SNR of the system's bispectral transfer function, a possible analytic approach would be to optimize this SNR for a finite number of frames. The SNR of the modulus of the bispectral transfer function for M statistically independent images is defined as

$$\mathrm{SNR}_M[\langle T^{(3)}(u,v)\rangle]=\frac{\mathrm{Mod}\,[\langle T^{(3)}(u,v)\rangle]}{\sigma_{\mathrm{B}}}\,\sqrt{M},\tag{17}$$

where σ_{B} is the standard deviation of the bispectral transfer function for a single image. A complicated integral expression for $\mathrm{SNR}_M[\langle T^{(3)}(u,v)\rangle]$ can be obtained using equation (15). Using this expression, optimal values of σ and ρ can, in principle, be calculated for strategically important values of u and v. Unfortunately, this theoretical approach is much more computer-intensive than finding the appropriate statistical parameters using a trial-and-error simulation approach. In addition, various sources of noise as well as different types of two-dimensional objects can easily be incorporated into the simulation to model a particular application. Due to these reasons, the trial-and-error simulation approach was chosen.
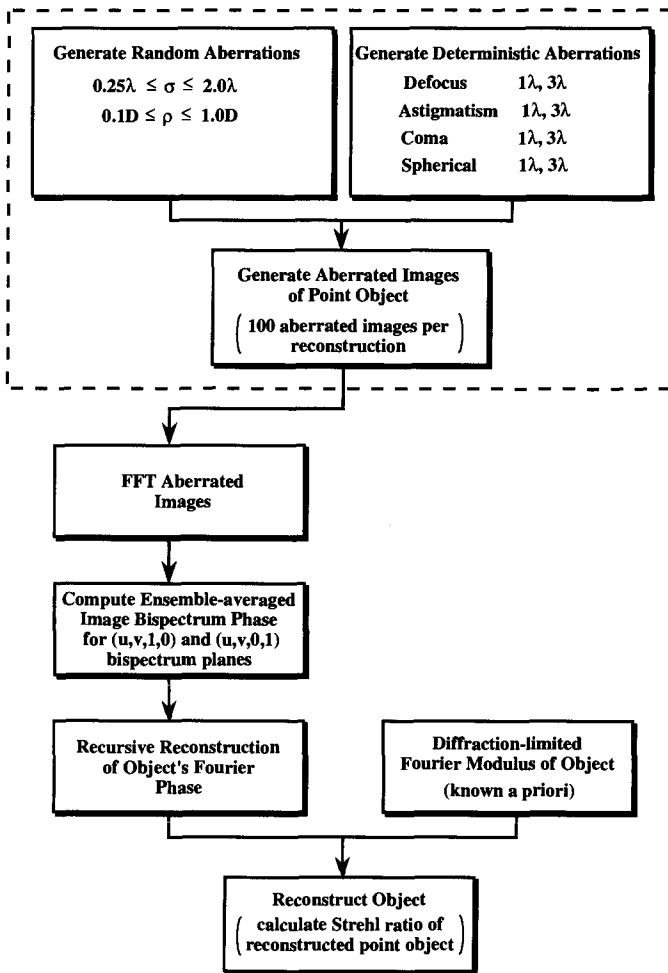
Figure 2. Flow chart of trial-and-error simulation showing the generation of the aberrated images as well as the reconstruction of the object using the bispectral imaging method.

3. Description of trial-and-error simulation

In the simulation, various amounts of random aberrations were added to an optical system containing a specified amount and type of deterministic aberrations. The values of σ and ρ of the random aberrations that resulted in the best reconstruction, using the bispectral imaging technique, were determined to be the optimal value. All objects used in the simulation were two-dimensional. A flow chart of the simulation is given in figure 2 showing the generation of the aberrated images as well as the reconstruction of the object using the bispectral imaging method.

The test object for the simulation was taken to be a point source, and the Strehl ratio was used as the figure of merit. The Strehl ratio is defined as the ratio of the light intensity at the peak of the diffraction pattern of an aberrated image to that at the peak of an aberration-free image [17]. Generally, an optical system is considered to be diffraction-limited if it has a Strehl ratio greater than 0·8. The simulation was done in the high-light-level region. In this region the effect of photon noise is negligible and therefore can be neglected. In the simulation, 100 statistically

independent aberrated images of the point source were used to estimate the point source's bispectrum. From equation (17) note that the SNR of the bispectral transfer function for M aberrated images is proportional to $\sqrt{M}$. Ayers *et al.* [18] and Nakajima [19] showed that the SNR of the bispectrum for a single aberrated image is proportional to r_0/D, where D is the diameter of the entrance pupil and r_0 is Fried's parameter, which is equal to the diameter of the diffraction-limited system whose Airy disc has the same area as the long-exposure point spread function of the aberrated system of diameter D; r_0 was first defined by Fried [20] and is a measure of image blurring caused by the random aberrations. Nakajima's result shows that the random aberrations are a noise source when estimating the bispectrum from a finite number of aberrated images, as is the case in this trial-and-error simulation.

The bispectral imaging technique was used to reconstruct the object's Fourier phase. We used the standard recursive algorithm to extract the diffraction-limited information of the object's Fourier phase from the bispectrum [10]. The recursive algorithm was chosen over other algorithms in the literature [21–23] due to its fast reconstruction capability. A fast reconstruction was highly desirable due to the large number of reconstructions needed in the simulation. The recursive algorithm directly utilizes the linear combination of object Fourier phases that make up the bispectrum phase. The $(u, v, 1, 0)$ and $(u, v, 0, 1)$ subplanes of the four-dimensional bispectrum were used in computing two estimates for each Fourier phase term of the object. The reconstructed Fourier phase was an average of the two estimates. Using other statistically independent subplanes of the bispectrum in the reconstruction would increase the SNR of the result in marginal signal situations, but would also increase the computation time.

The reconstructed Fourier phase was then combined with the diffraction-limited Fourier modulus of the object. Techniques are available to reconstruct the object's Fourier modulus, such as stellar speckle interferometry [24]. We were solely interested in the performance of the bispectral imaging technique and therefore did not want errors in the reconstructed Fourier modulus to affect the results. Consequently, we assumed *a priori* knowledge of the diffraction-limited Fourier modulus.

In the simulation, each image was represented by a 128×128 complex array. The diameter of the circular pupil, representing the pupil of the optical system, was 64 pixels. The rectangular sample grid produced small artifacts in the images, such as a slight loss in the circular symmetry of the imaged point source. This artifact is more apparent in the diffraction-limited case than when the system contains circularly symmetric aberrations such as defocus or spherical aberration.

The deterministic aberrations used in the simulation were defocus, and third-order coma, astigmatism, and spherical aberration. Astigmatism and coma were considered in the isoplanatic case. The four aberrations were evaluated at strengths of 1λ and 3λ, where λ is the wavelength of the incident light. By analysing the simulation-generated blurred images resulting from imaging the point source through systems having these aberrations at strengths of 1λ and 3λ, as well as the diffraction-limited case, we empirically found that aliasing errors in the blurred images, due to sampling of the wavefront in the pupil plane, were negligible.

The random aberrations, which multiply the wavefront by the phase factor $\exp(\mathrm{i}kZ(u))$, were generated in the following manner. Each realization of a zero-mean, Gaussian-distributed, delta-correlated random process was generated in a 512×512 complex array using a Gaussian random number generator based on a

subtractive method [25]. As was previously defined in equation (8), σ^2 is the variance of the Gaussian distribution of the random process. Each realization was then convolved with an appropriate Gaussian function to make zero-mean, Gaussian-distributed, Gaussian-correlated random aberrations; $\rho^2/2$ is the variance of the convolving Gaussian function and $\sqrt{(2)}\rho$ was previously defined in equation (9) as the correlation length of the random aberrations. The convolving Gaussian function was given in a 512×512 complex array and was specified out to three standard deviations. The remaining part of the 512×512 complex array was padded with zeroes. Only a 64×64 section of the 512×512 zero-mean, Gaussian-distributed, Gaussian-correlated complex array was used to represent the random aberrations in the simulation. Using such a small section of the 512×512 complex array enabled ρ to extend up to one pupil diameter (64 pixels) without any wrap-around artifacts. In the simulation, σ ranged from $0.25\,\lambda$ to $2.00\,\lambda$ in increments of $0.25\,\lambda$. Likewise, ρ ranged from $0.1\,D$ to $1.0\,D$ in increments of $0.1\,D$, where D is the diameter of the system's pupil. This resulted in 80 data points covering a wide range of σ and ρ values.

Figure 3 contains a contour plot of the Strehl ratio of the long-exposure point spread function (PSF) as a function of σ and ρ. The long exposure is defined here as a direct ensemble average of the 100 distorted images. Certain strengths did result in noticeable amounts of aliasing in the blurred images due to undersampling in the pupil plane. In particular, noticeable aliasing occurred for $\sigma = 1.25\,\lambda$ and $\rho = 0.1\,D$, $\sigma = 1.50\,\lambda$ and $\rho = 0.1\,D$, $\sigma = 1.75\,\lambda$ and $\rho = 0.1\,D$, and $\sigma = 2.00\,\lambda$ and $\rho = 0.1\,D$; these four σ–ρ values produced the most image blurring and correspond to values in the upper left of the contour plot. The Strehl ratios for the other values range from 0.003 to 0.767. When converted to the Kolmogorov model [26], the random aberrations have D/r_0 values approximately ranging from 0.6 to 22. This clearly indicates the wide range of random aberration strengths used in the simulation.

Figure 4 illustrates the accuracy of the random aberrations generated in the computer simulation. The figure shows several modulation transfer function (MTF) curves of the simulated data as well as corresponding theoretical MTF curves for the diffraction-limited case, $\sigma = 0.25\,\lambda$ and $\rho = 1.0\,D$, $\sigma = 0.75\,\lambda$ and $\rho = 0.7\,D$, and $\sigma = 1.50\,\lambda$ and $\rho = 0.2\,D$. The MTF curves of the simulated data were generated by taking the modulus of the Fourier transform of the long exposure PSFs. The theoretical MTFs were obtained using [27]

$$\text{Mod}\,[H(u)] = H_0(u)\exp\left[-\sigma^2\left(1 - \exp\left[-\frac{u}{2\rho^2}\right]\right)\right], \tag{18}$$

where $H_0(u)$ is the diffraction-limited MTF. Equation (18) was derived for the case of a thin random-phase screen located at the pupil of the system that was Gaussian-distributed and Gaussian-correlated. Excellent agreement is found between the simulated and theoretical results for MTF values above 0.02.

4. Results of trial-and-error simulation

4.1. *Systems with only random aberrations*

In the simulation, reconstructions of a point object were first obtained for systems containing only random aberrations having various values of σ and ρ. These reconstructions indicate the ability of the bispectral imaging method to overcome the distorting effects of the random aberrations. They represent an upper limit for
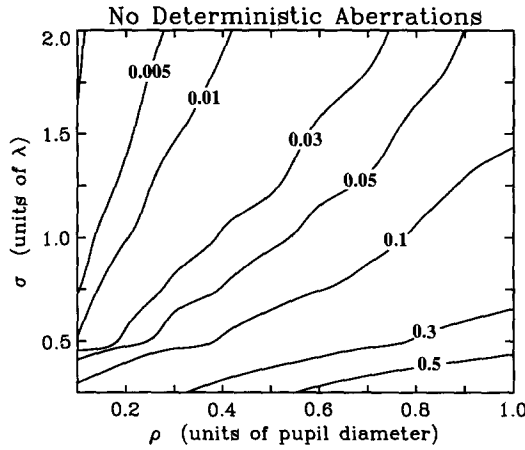
No Deterministic Aberrations

Figure 3. Contour map of the long exposure Strehl ratios drawn on the σ–ρ plane. No deterministic aberrations were present in the system.
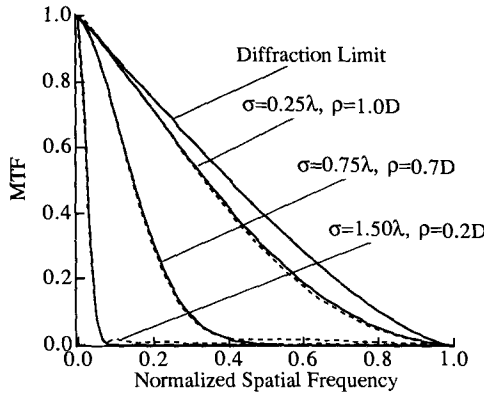
Figure 4. Modulation transfer functions for various strengths of the random aberrations, including the diffraction-limited case; (———) theoretical results, (- - -) simulated results, based on one hundred realizations.

the reconstructed Strehl ratio when the system contains both random and deterministic aberrations. This upper limit is evident in the analytic expression of the bispectral transfer function given by equation (15). In equation (15) the deterministic aberrations contribute to the bispectral transfer function through the second exponential term in the integrand. When there are no deterministic aberrations in the system, this second term is equal to unity, and therefore the transfer function is completely characterized by the random aberrations and the size of the pupil. When deterministic aberrations are present, however, this second term is a complex exponential that causes a reduction in the magnitude of the bispectral transfer function and therefore a reduction in the bispectral transfer function's SNR. This lower SNR in turn causes the reconstructed Strehl ratio to be lower than that of the no-deterministic-aberration case.

Using the bispectral imaging method on systems containing only random aberrations, the Strehl ratios of the reconstructions for various values of σ and ρ are
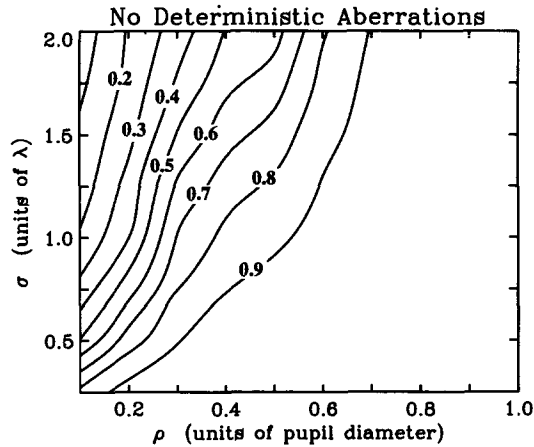
Figure 5. Contour map of the reconstructed Strehl ratios drawn on the $\sigma-\rho$ plane. No deterministic aberrations were present in the system.

shown in the contour plot of figure 5. These reconstructions show a significant improvement over the long exposure results given in the contour plot of figure 3. The long-exposure results are not considered to be diffraction-limited since their Strehl ratios are all less than 0·8. In fact, 87% of the long exposures have a Strehl ratio below 0·3. However, by using the bispectral imaging method, 65% of the reconstructions in figure 5 are considered to be diffraction-limited.

For illustrative purposes, the long-exposure and reconstructed images are shown in figure 6. In the figure the centre 64×64 pixel areas of the 128×128 pixel images are displayed on a $\sigma-\rho$ plot. The position of each individual image on the $\sigma-\rho$ plot is determined by the values of σ and ρ used in generating that particular image. Figure 6 displays the long-exposure and reconstructed images on two separate $\sigma-\rho$ plots. To facilitate comparison, all images in figure 6 were scaled to have the same maximum intensity value. These results vividly illustrate the power of the bispectral imaging method to unscramble images distorted by random aberrations. Its usefulness to the astronomy community is quite evident.

4.2. *Systems with random aberrations and three waves of deterministic aberrations*

The deterministic aberrations used in the simulation were defocus, and third-order astigmatism, coma, and spherical aberration. For systems with three waves of either defocus, astigmatism, coma, or spherical aberration, the corresponding Strehl ratios are 0·01, 0·06, 0·09, and 0·03, respectively. These values are given in the third column of table 1. The small size of these Strehl ratios clearly indicates the large strength of the deterministic aberrations.

The random aberrations used in section 4.1 were then combined with these deterministic aberrations. In this case the system contained random aberrations having various values of σ and ρ, and three waves of either defocus, astigmatism, coma, or spherical aberration. Four contour plots of the Strehl ratios of the reconstructions using the bispectral imaging method are given in figure 7. Comparing the three $\sigma-\rho$ contour plots containing the even aberrations in figure 7 with the Strehl ratios given in the third column of table 1, one finds that many of the reconstructed Strehl ratios are significantly larger than those of the original
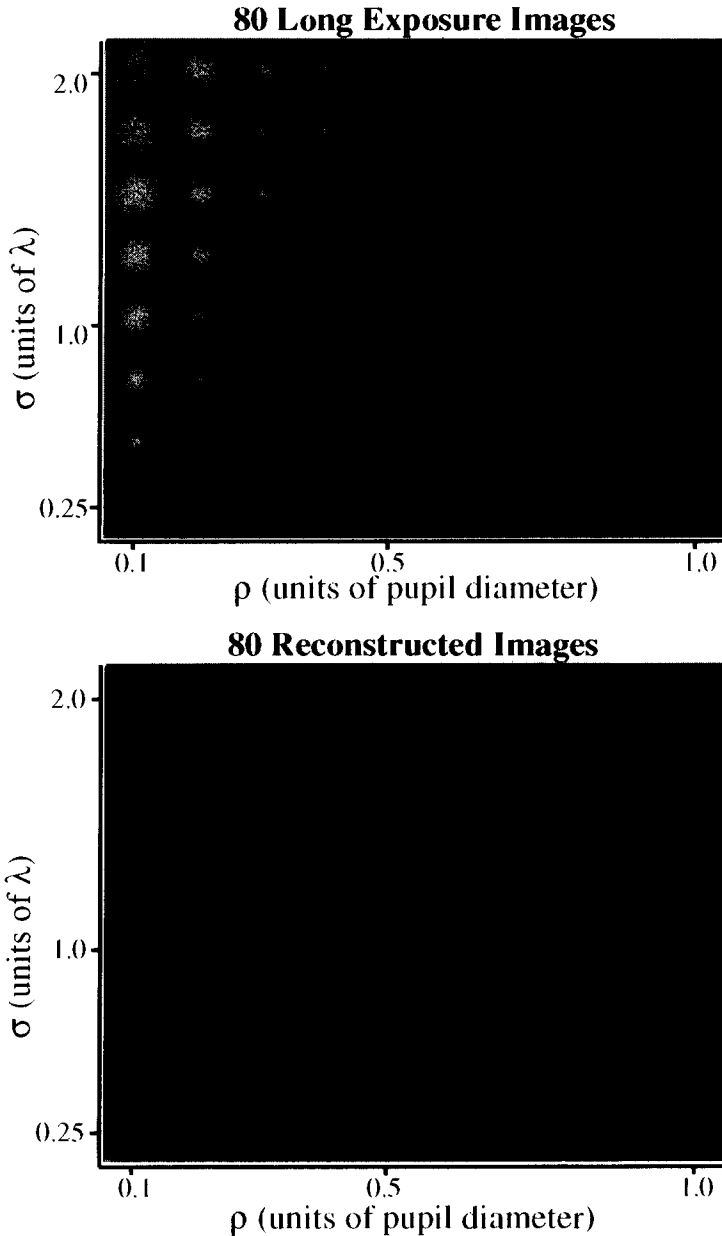
80 Long Exposure Images

80 Reconstructed Images

Figure 6.   Top image contains the long exposure images displayed on the $\sigma-\rho$ plane; bottom image contains the reconstructed images using the bispectral imaging method displayed on the $\sigma-\rho$ plane. Each individual image represents the long exposure or reconstructed point spread function of the system for particular values of σ and ρ. The system contains random aberrations whose strength is specified by σ and ρ and no deterministic aberrations. Each of the individual images displayed on the $\sigma-\rho$ planes is the centre 64×64 pixel subsection of the original 128×128 pixel image.

Table 1. Strehl ratios for systems containing three waves of defocus, astigmatism, coma, and spherical aberration. The third column contains the Strehl ratios for systems with only deterministic aberrations present. The fourth column contains the maximum reconstructed Strehl ratios found in the contour plots of figure 7, along with the corresponding values of σ and ρ. For the even-order aberrations, note the significant improvement of the reconstructed Strehl ratios using the bispectral method compared to the Strehl ratios for systems with only deterministic aberrations.

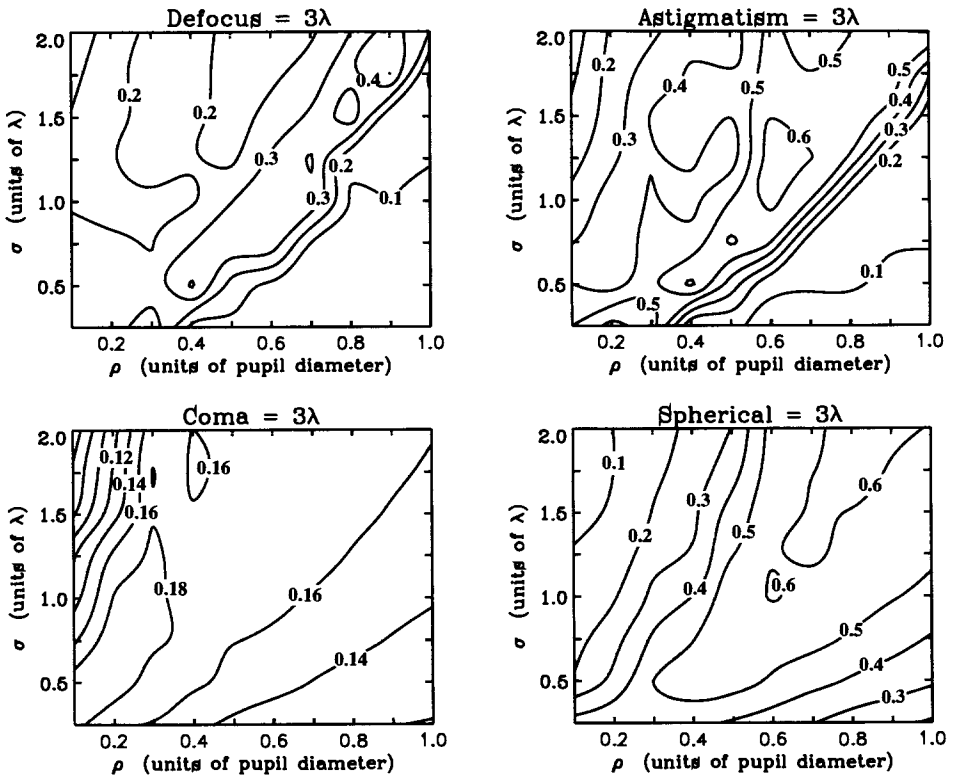| Deterministic aberrations	Size of aberrations	Strehl ratio for stystem with deterministic aberrations	Maximum reconstructed Strehl ratio
W_{020}	3λ	0·01	0·50 ($\sigma = 1{\cdot}75\,\lambda$, $\rho = 0{\cdot}9\,D$)
W_{022}	3λ	0·06	0·65 ($\sigma = 1{\cdot}25\,\lambda$, $\rho = 0{\cdot}6\,D$)
W_{031}	3λ	0·09	0·20 ($\sigma = 1{\cdot}25\,\lambda$, $\rho = 0{\cdot}6\,D$)
W_{040}	3λ	0·03	0·63 ($\sigma = 2{\cdot}00\,\lambda$, $\rho = 0{\cdot}8\,D$)

Figure 7. Four contour maps of the reconstructed Strehl ratios drawn on the σ–ρ plane. The deterministic aberrations present in the system were three waves of defocus, astigmatism, coma, and spherical aberration.

system containing only the deterministic aberrations. This suggests that many of the zero points in the bispectral transfer function due to the deterministic aberrations have been eliminated by introducing random aberrations into the system. In addition, it indicates that the SNR of the $(u, v, 1, 0)$ and $(u, v, 0, 1)$ planes in the image bispectrum remained acceptable after the random aberrations were introduced.

For the odd aberration coma, the results in figure 7 are quite different. The reconstructed Strehl ratios show only a modest increase over that of the original system containing only the deterministic aberration. Like the even aberrations, coma can introduce zero points into the bispectral transfer function. In addition though, it also introduces a non-zero phase into the bispectral transfer function. The results of figure 7 suggest that this non-zero phase is not eliminated from the bispectral transfer function when random aberrations are introduced into the system.

From the three σ–ρ contour plots containing the even aberrations in figure 7, the best reconstructions occur along a diagonal line roughly through the centre of the plots; this is an interesting result. It shows that introducing very weak random aberrations (lower-right section of contour plots) into the system results in very poor reconstructions. In this region the deterministic aberrations dominate and therefore limit the quality of the reconstruction. In the analytic expression of the bispectral transfer function given by equation (15), this corresponds to the second exponential term in the integrand being the dominating component in the integrand. In this case the first exponential term, which contains the random aberrations, does not decay sufficiently to eliminate the zero points in the bispectral transfer function that are caused by the deterministic aberrations , in the second exponential term. Thus, poor reconstructions are obtained that are similar in quality to those for systems containing only deterministic aberrations. When very strong random aberrations (upper-left section of contour plots) are introduced into the system, poor reconstructions are also obtained. In this region the random aberrations are now the dominating component, and therefore limit the quality of the reconstruction. In equation (15) this corresponds to the first exponential term in the integrand being the dominating component in the integrand. In this case the zero points in the bispectral transfer function are essentially eliminated by the first term due to the first term's strong exponentially decaying behaviour. However, this first term decays so rapidly that the resulting magnitude of the bispectral transfer function becomes too small. In this case the noise generated from estimating this small magnitude from 100 aberrated images becomes the main limiting factor in the quality of the reconstructed object. Along a diagonal line through the centre of the plots, however, a compromise is achieved between the detrimental effects of the random and deterministic aberrations. In this region the combined image-degrading effects of the random and deterministic aberrations within the bispectral transfer function are minimized, thus producing the best reconstructions. In equation (15) this corresponds to the first exponential term exponentially decaying fast enough to eliminate many (but possibly not all) of the zeroes in the bispectral transfer function caused by the second term, yet decaying slow enough for the bispectral transfer function's magnitude to stay at an acceptable level above the noise.

The last column of table 1 contains the maximum Strehl ratios found in the reconstructed Strehl ratios in figure 7 for each of the four deterministic aberrations. From table 1 one finds that the bispectral imaging method was unable to produce diffraction-limited reconstructions. Image quality, however, did improve

significantly for systems with even aberrations. In comparing columns three and four of table 1, note that the reconstructed Strehl ratios using the bispectral imaging method were 10–50 times larger than those for systems with only deterministic aberrations. This is a dramatic improvement in image quality. For the odd aberration, however, an increase of only a factor of two was obtained.

For illustrative purposes, the long exposure and reconstructed images for the defocus and astigmatic cases are shown on the σ–ρ plots in figures 8 and 9, respectively. In the long-exposure images, notice the upper-left and lower-right sections of the σ–ρ plots where the effect of the random and deterministic aberrations dominate each other. These two regions are separated by a transition region where the best reconstructions are found. Finally, note the extreme difference in image quality between the long-exposure and reconstructed images. The benefit of introducing random aberrations into a system with deterministic aberrations and then applying the bispectral imaging method is quite clear.

4.3. *Systems with random aberrations and one wave of deterministic aberrations*

For systems with one wave of either defocus, astigmatism, coma, or spherical aberration, the corresponding Strehl ratios are 0·05, 0·23, 0·53, and 0·09, respectively. These values are given in the third column of table 2. The random aberrations used in section 4.1 were then combined with these deterministic aberrations. In this case the system contained random aberrations having various values of σ and ρ, and one wave of either defocus, astigmatism, coma, or spherical aberration. Four contour plots of the Strehl ratios of the reconstructions using the bispectral imaging method are given in figure 10. The last column of table 2 contains the maximum Strehl ratios found in the σ–ρ plots of figure 10. In these contour plots, the largest reconstructed Strehl ratios generally occur when weak random aberrations (lower-right section of contour plots) are present in the system. This is in sharp contrast to the results of section 4.2 that are given in figure 7. In figure 7, the best reconstructions occur along a diagonal line through the centre of the σ–ρ plots.

Note that in the σ–ρ contour plot containing the odd aberration coma in figure 10, the reconstructed Strehl ratios show at best only a modest increase over that of the original system containing only the deterministic aberration. The maximum reconstructed Strehl ratio is 0·64, which is an increase of only 0·11 over that of the deterministic-aberration-only case. For the three even aberrations, however, the results are quite different. Most of the reconstructed Strehl ratios are significantly larger than those of the deterministic-aberration-only case. The largest Strehl ratio obtained for each of the even aberration cases ranged from 0·90 to 0·95. The results show that introducing all but the very strong random aberrations produces significant improvement when even aberrations are present. Better still, diffraction-limited reconstructions were obtained over a large range of σ and ρ values. Fortunately, these diffraction-limited regions overlap significantly. This implies that by choosing a random aberration that falls within the overlapping diffraction-limited regions in the σ–ρ space, one can obtain a diffraction-limited reconstruction when the system has one wave or less of defocus, astigmatism, or spherical aberration.

To illustrate this result, an extended real object was reconstructed that had been blurred by one wave of either defocus, astigmatism, or spherical aberration. Random aberrations having $\sigma = 0·75\lambda$ and $\rho = 1·0D$ were added to the system. From
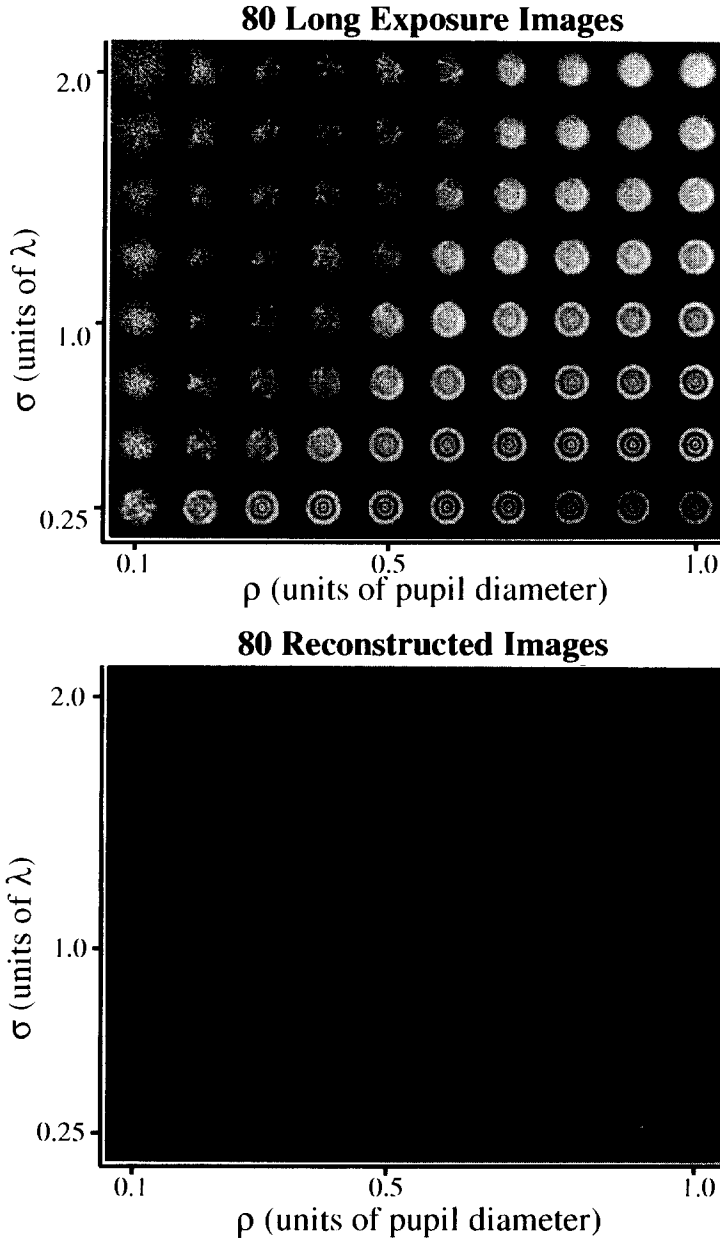
80 Long Exposure Images

80 Reconstructed Images

Figure 8. Top image contains the long exposure images displayed on the σ–ρ plane; bottom image contains the reconstructed images using the bispectral imaging method displayed on the σ–ρ plane. Each individual image represents the long exposure or reconstructed point spread function of the system for particular values of σ and ρ. The system contains random aberrations whose strength is specified by σ and ρ and three waves of defocus. Each of the individual images displayed on the σ–ρ planes is the centre 64×64 pixel subsection of the original 128×128 pixel image.
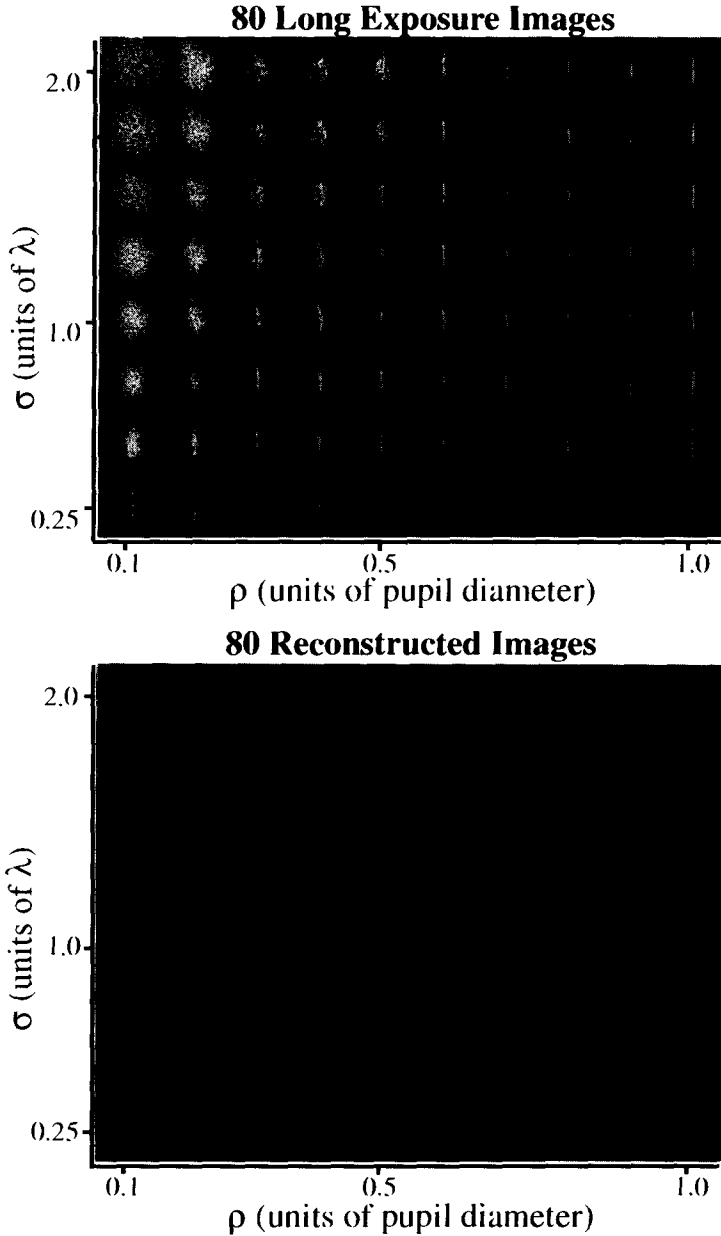
Figure 9. Top image contains the long exposure images displayed on the $\sigma-\rho$ plane; bottom image contains the reconstructed images using the bispectral imaging method displayed on the $\sigma-\rho$ plane. Each individual image represents the long exposure or reconstructed point spread function of the system for particular values of σ and ρ. The system contains random aberrations whose strength is specified by σ and ρ and three waves of astigmatism. Each of the individual images displayed on the $\sigma-\rho$ planes is the centre 64×64 pixel subsection of the original 128×128 pixel image.

Table 2. Strehl ratios for systems containing one wave of defocus, astigmatism, coma, and spherical aberration. The third column contains the Strehl ratios for systems with only deterministic aberrations present. The fourth column contains the maximum reconstructed Strehl ratios found in the contour plots of figure 10 along with the corresponding values of σ and ρ. For the even-order aberrations, note the significant improvement of the reconstructed Strehl ratios using the bispectral method compared to the Strehl ratios for systems with only deterministic aberrations.

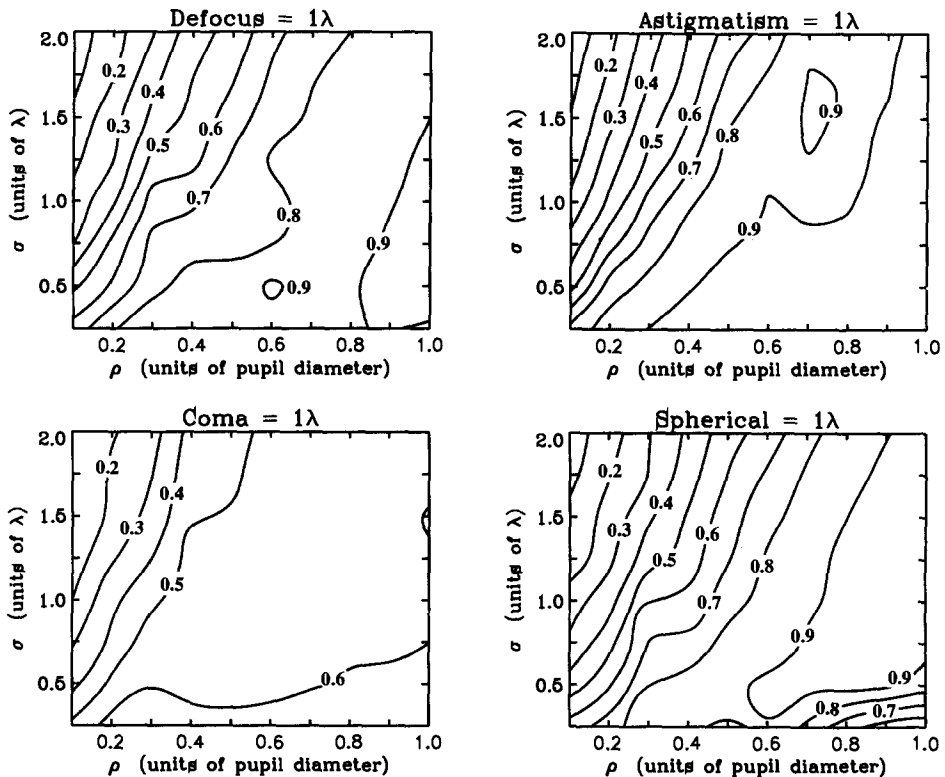| Deterministic aberrations	Size of aberrations	Strehl ratio for system with deterministic aberrations	Maximum reconstructed Strehl ratio
W_{020}	1λ	0·05	0·94 ($\sigma = 0·50\lambda$, $\rho = 1·0D$)
W_{022}	1λ	0·23	0·96 ($\sigma = 0·50\lambda$, $\rho = 1·0D$)
W_{031}	1λ	0·53	0·64 ($\sigma = 0·25\lambda$, $\rho = 0·2D$)
W_{040}	1λ	0·09	0·95 ($\sigma = 1·50\lambda$, $\rho = 1·0D$)

Figure 10. Four contour maps of the reconstructed Strehl ratios drawn on the σ–ρ plane. The deterministic aberrations present in the system were one wave of defocus, astigmatism, coma, and spherical aberration.
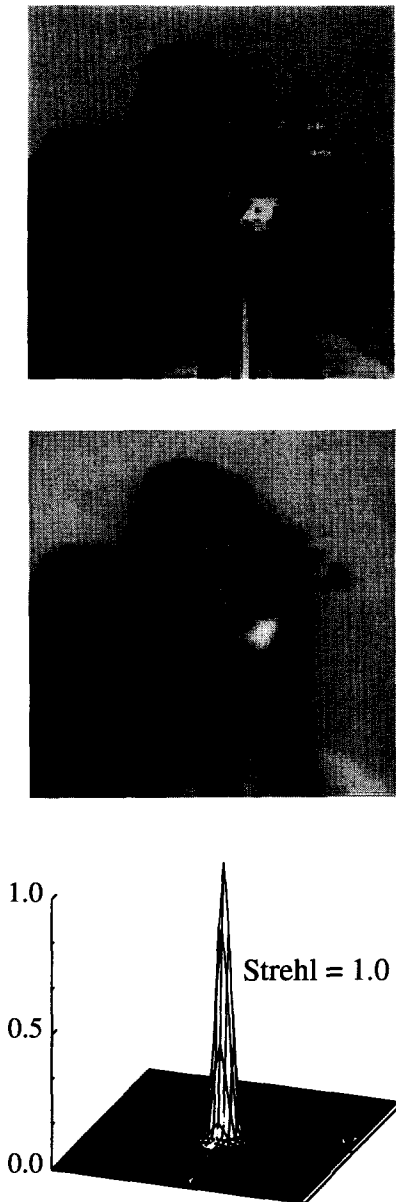
Figure 11. Top image is the original 128×128 extended object; below it is the diffraction-limited image of the object, as well as a surface plot of the diffraction-limited point spread function of the system. The diffraction-limited image is noticeably blurred due to a small pupil diameter.

figure 10 this strength of the random aberrations falls within the overlapping diffraction-limited regions, and thus should produce diffraction-limited reconstructions. The original 128×128 object is shown at the top of figure 11. Below it is the diffraction-limited image of the object as well as a surface plot of the diffraction-limited point spread function of the system. The diffraction-limited image is noticeably blurred

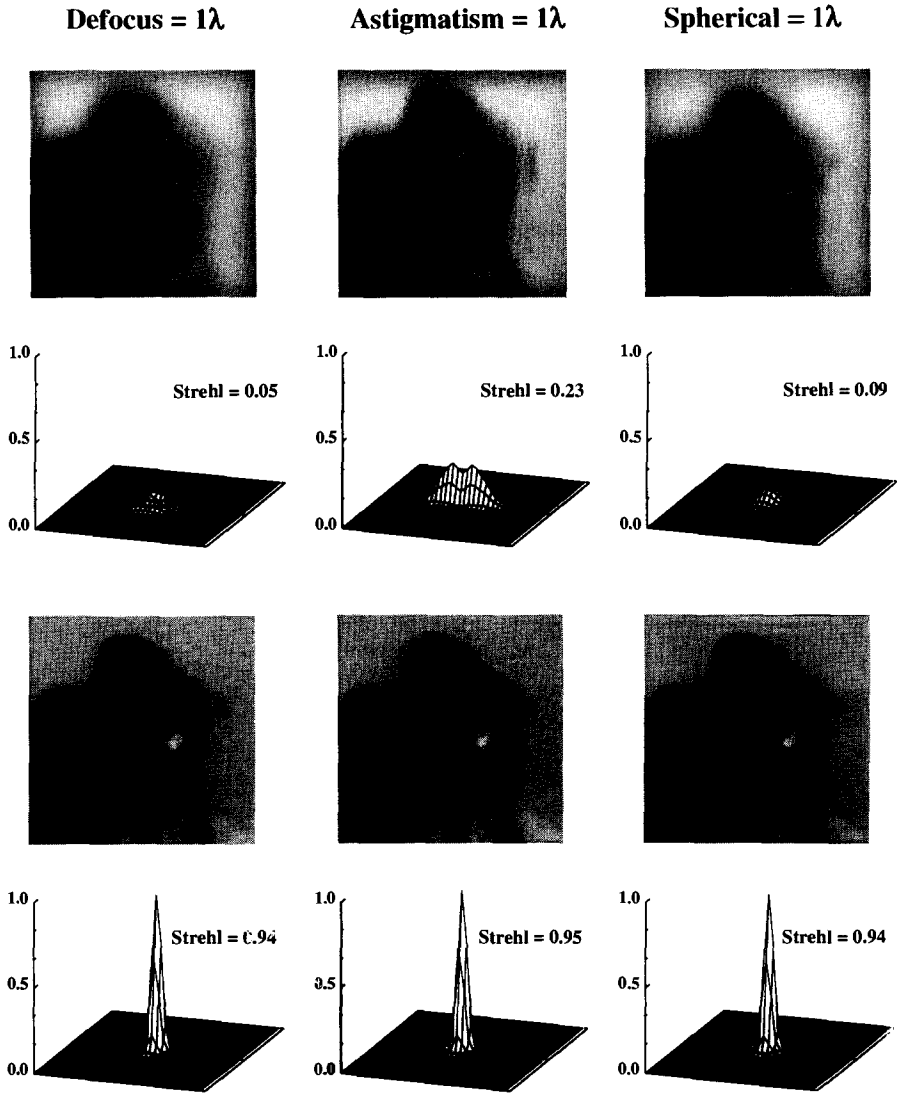**Defocus = 1λ**   **Astigmatism = 1λ**   **Spherical = 1λ**

Figure 12.   Top row contains original blurred images of the extended object, which is shown in figure 11. The object was blurred by one wave of either defocus, astigmatism, or spherical aberration. Surface plots of the associated point spread functions for the aberrated system are given in the second row. The third row contains the reconstructed images after random aberrations, having $\sigma = 0.75\,\lambda$ and $\rho = 1.0\,D$, were added to the system. Surface plots of the reconstructed point spread functions are given in the last row.

due to a pupil diameter of only 64 pixels. This diameter was chosen in order to use the realizations of the random aberrations previously generated in section 3.

The results are shown in figure 12. The top row contains the original blurred images of the extended object. The object was blurred by one wave of either defocus, astigmatism, or spherical aberration. Surface plots of the associated point spread functions for the aberrated system are given in the second row. The third row

contains the reconstructed images after random aberrations, having $\sigma = 0.75\,\lambda$ and $\rho = 1.0\,D$, were added to the system. The Fourier phase was reconstructed using the bispectral imaging method and the Fourier modulus was assumed to be known *a priori*. Surface plots of the reconstructed point spread functions are given in the last row. From figure 12 the reconstructed images are significantly better than the original blurred images and, in comparing the reconstructions to the diffraction-limited image of figure 11, are considered near-diffraction-limited.

5. Summary

We have investigated the bispectral imaging method as a technique for de-blurring an image that is formed from a system with unknown aberrations. Through computer simulations we have found the optimal amount of random aberrations to have present in a system containing certain types and amounts of deterministic aberrations—this amount optimizes the Strehl ratio of the reconstruction at high light levels.

In particular the following conclusions can be made. The method was found to work well in reconstructing images for systems with even aberrations such as defocus, astigmatism, and spherical aberration. Poor reconstructions however were obtained for systems with the odd aberration coma. Secondly, from the results shown in figures 7 and 10, it was found that the optimal values of σ and ρ depend in a complicated manner upon the type and amount of deterministic aberrations present in the system. Though this dependency is complicated, important practical and useful results can be extracted. For example, it was found that diffraction-limited reconstructions are possible over a wide range of σ and ρ values for systems with one wave or less of either defocus, astigmatism, or spherical aberration. In addition, these diffraction-limited regions were found to overlap significantly. For applications utilizing this method, this is an important result; it permits easier fabrication of the random aberrations due to the larger tolerances on σ and ρ. More importantly, knowledge of the precise amount of deterministic aberrations in the system is not required. To assure oneself of a diffraction-limited result, the results in figures 10 and 12 indicate that one only needs to know that the system under study contains one wave or less of either defocus, astigmatism, or spherical aberration.

These results indicate that the bispectral imaging method is a promising technique for de-blurring an image that is formed from a system with unknown aberrations at high light levels. Its applicability to reconstructing high-resolution images of the eye's fundus in human subjects is currently being investigated. The effect of noise sources, such as photon and read noise, on the bispectral method's reconstruction capability in the presence of random and deterministic aberrations is also being examined.

References

[1] BATES, R. H. T., and McDONNELL, M. J., 1989, *Image Restoration and Reconstruction* (Oxford: Oxford University Press).

[2] TSUJIUCHI, J., 1963, *Progress in Optics*, Vol. II, edited by E. Wolf (Amsterdam: North-Holland).

[3] INDEBETOUW, G., 1990, *Appl. Optics*, **29**, 5262–5267.

[4] BAKUT, P. A., RYAKHIN, A. D., and SVRIDOV, K. N., 1987, *Opt. Spectrosc.* (USSR), **63**, 683–685.

[5] BARAKAT, R., and EBSTEIN, S., 1987, *J. opt. Soc. Am.* A, **4**, 1756–1763.

[6] CEDERQUIST, J. N., FIENUP, J. R., MARRON, J. C., SCHULZ, T. J., and SELDIN, J. H., 1991, *SPIE Proc.*, **1416**, 266–277.

[7] PAXMAN, R. G., SCHULZ, T. J., and FIENUP, J. R., 1992, *J. opt. Soc. Am.* A, **9**, 1072–1085.

[8] SEZAN, M. I., and TEKALP, A. M., 1990, *Opt. Engng.*, **29**, 393–404.

[9] RODDIER, F., 1986, *Optics Commun.*, **60**, 145–148.

[10] LOHMANN, A., WEIGELT, G., and WIRNITZER, B., 1983, *Appl. Optics*, **22**, 4028–4037.

[11] ZHANG, J.-Y., and DAINTY, J. C., 1992, *J. mod. Optics*, **39**, 2383–2404.

[12] WEIGELT, G., BAIER, G., EBERSBERGER, J., FLEISCHMANN, F., HOFMANN, K. H., and LADEBECK, R., 1986, *Opt. Engng.*, **25**, 706–711.

[13] CHARMAN, W. N., 1991, *Optom. Vis. Sci.*, **68**, 574–583.

[14] CAMPBELL, M. C. W., HARRISON, E. M., and SIMONET, P., 1990, *Vision Res.*, **30**, 1587–1602.

[15] GOODMAN, J. W., 1985, *Statistical Optics* (New York: Wiley) pp. 374–384.

[16] WELFORD, W. T., 1986, *Aberrations of Optical Systems* (Bristol: Adam Hilger), pp. 130–140.

[17] SMITH, W. J., 1966, *Modern Optical Engineering* (New York: McGraw-Hill).

[18] AYERS, G. R., NORTHCOTT, M. J., and DAINTY, J. C., 1988, *J. opt. Soc. Am.* A, **5**, 963–985.

[19] NAKAJIMA, T., 1988, *J. opt. Soc. Am.* A, **5**, 1477–1491.

[20] FRIED, D. L., 1966, *J. opt. Soc. Am.*, **56**, 1372–1379.

[21] NEWMAN, D., and VAN VRANKEN, R. C., 1992, *J. opt. Soc. Am.* A, **9**, 1724–1739.

[22] MATSON, C. L., 1991, *J. opt. Soc. Am.* A, **8**, 1905–1913.

[23] HANIFF, C. A., 1991, *J. opt. Soc. Am.* A, **8**, 134–140.

[24] LABEYRIE, A., 1970, *Astron. Astrophys.*, **6**, 85–87.

[25] PRESS, W. H., FLANNERY, B. P., TEUKOLSKY, S. A., and VETTERLING, W. T., 1988, *Numerical Recipes in C* (New York: Cambridge University Press), pp. 212–213, 216–217.

[26] BARAKAT, R., and NISENSON, P., 1981, *J. opt. Soc. Am.*, **71**, 1390–1402.

[27] GOODMAN, J. W., 1985, *Statistical Optics* (New York: Wiley), p. 379.